metals

MDPI

Communication

Microstructure and Properties of Non-Equiatomic $Ni_{10}Cr_6WFe_9TiAlx$ High-Entropy Alloys Combined with High Strength and Toughness

Xigang Yang [1,*,†], Lin He [2,†], Erhong Li [2] and Chenglong Yang [2]

[1] School of Materials Science and Chemical Engineering, Xi'an Technological University, Xi'an 710021, China
[2] Shanxi North Casting Co., Ltd., Datong 037036, China
* Correspondence: xgyang@xatu.edu.cn
† These authors contributed equally to this work.

Abstract: High-entropy alloys (HEAs) with excellent mechanical properties have broad application scope and application prospects. However, it is difficult to obtain the optimized element composition, based on the traditional equiatomic or near-equiatomic statistical analysis of the phase selection rules. The non-equiatomic HEAs have abundant constituents combination by optimizing the type and content of elements. In this study, $Ni_{10}Cr_6WFe_9TiAlx$ (x = 0, 1.0 and 1.5, at.%) HEAs were prepared by vacuum arc melting. The effect of Al content x on microstructure and mechanical properties of HEAs was systematically studied. The results show that the HEAs are composed mainly of face-centered cubic (FCC) with hexagonal Al_2W phase. The increase of Al content promotes the formation of the hexagonal Al_2W phase. When the Al mole content is 1.0, the $Ni_{10}Cr_6WFe_9TiAl$ HEA material has achieved superior mechanical properties. The alloy exhibited a high ultimate tensile strength of 741 MPa and a large total elongation of 46%. The improvement in the mechanical properties of the $Ni_{10}Cr_6WFe_9TiAl$ HEA is mainly attributed to the precipitation strengthening of the high-density Al_2W phase. This work provides a reference for the future design of Al_2W precipitation-strengthened non-equiatomic HEAs with ideal properties.

Keywords: $Ni_{10}Cr_6WFe_9TiAl$ high-entropy alloys; non-equiatomic high-entropy alloys; microstructure; mechanical properties

Citation: Yang, X.; He, L.; Li, E.; Yang, C. Microstructure and Properties of Non-Equiatomic $Ni_{10}Cr_6WFe_9TiAlx$ High-Entropy Alloys Combined with High Strength and Toughness. *Metals* **2023**, *13*, 1179. https://doi.org/10.3390/met13071179

Academic Editor: Jiro Kitagawa

Received: 23 May 2023
Revised: 19 June 2023
Accepted: 20 June 2023
Published: 25 June 2023

1. Introduction

High-entropy alloys (HEAs), as a newly developed metallic material, are composed of multiple constituents in concentrations ranging from 5~35 at.%. Owning to their unique chemical complexity caused by random distribution of elements in lattice, these alloys exhibit excellent mechanical properties, e.g., high strength, hardness, excellent ductility, and extreme softening resistance at elevated temperatures, which are believed to originate from their high configurational entropy and severe lattice distortion [1–4]. Compared to conventional alloys with one principle element, the underlying principle of multicomponent HEAs is endowed with an abundant constituents combination, that is, thousands of alloys will be synthesized by changing the type and content of elements, and the crystal structure, microstructure, and mechanical properties will undergo significant changes [5–7]. However, due to the lack of theoretical predictions and simulations of HEAs, the current research mainly focuses on the microstructure and physical properties of equiatomic or near-equiatomic HEAs [8–10], and improving performances of these HEAs is quite limited. Due to the limited regulating composition range to optimize the alloy microstructures, the competitive advantages of the multicomponent have not yet been fully exploited. In addition, the high-strength and -toughness HEAs systems are quite limited, and the exploration of new high-strength and -toughness HEAs in broader alloy systems is still an unsolved

challenge [11,12]. In these cases, it is necessary to explore non-equiatomic HEA systems to develop their latent value.

Design and development of the non-equiatomic HEAs with excellent strength and toughness has been the focus of many studies in recent years. One approach to solving these issues is the adding or variation of alloying elements (e.g., titanium (Ti), aluminum (Al), silicon (Si), and copper (Cu)) to equiatomic or near-equiatomic HEAs, which can effectively improve combination properties, while maintaining simple solid solution phases [13–19]. Hu et al. [15] used the powder metallurgy technique to study microstructure and corrosion properties of AlxCuFeNiCoCr (x = 0.5, 1.0, 1.5, 2.0) high-entropy alloys, and the results confirmed that the microstructure and corrosion properties of these alloys are closely related to its Al content. Chuang et al. [18] showed that the $Al_xCo_{1.5}CrFeNi_{1.5}Tiy$ HEAs with a high Ti/Al ratio showed higher wear resistance compared with the conventional wear-resistant steels. In addition, several studies have demonstrated that the excellent properties are not unique to the equiatomic composition, and there is a high chance that even better properties are obtained at non-equiatomic compositions, such as $Al_{0.5}NbTi_3V_xZr_2$, $Fe_3Cr_2Al_2CuNi_4Si_5$, and $Ni_6Cr_4WFe_9Ti$ [5,6,19–25]. Although many HEAs have been developed, theoretical predictions and simulations of HEAs are still lacking due to their chemical complexity. Therefore, the component design of non-equiatomic HEAs has not been solved well. Unlike any equiatomic or near-equiatomic HEAs, non-equiatomic HEAs has thousands upon thousands of alloy compositions by changing the type and content of elements, which provide ample opportunities to design and tune the phase composition and properties. In addition, by making full use of the advantage of high-entropy effect (inhibit compound phases) in HEAs, developing of non-equiatomic HEAs with excellent mechanical properties has important realistic significance for broadening alloy compositions.

In a previous study, we designed a novel non-equiatomic $Ni_{10}Cr_6WFe_9Ti$ HEA with FCC structure using arc smelting, which exhibited ultimate ductility of over 50%, and tensile strength of the alloy has only 650 MPa (although this alloy is prepared by additive manufacturing, which exhibited excellent mechanical properties with the ultimate tensile strength (σUTS) of ~962 MPa and a total elongation (ε) of ~21.6% at room temperature [26]). To the best of our knowledge, no similar composition design has been established so far for the non-equiatomic NiCrWFeTi series HEAs, and the understanding of the phase stability and mechanical of these HEAs is very limited. In this paper, we are attempting to fulfill the gap by doping metal elements in the non-equiatomic NiCrWFeTi series HEAs forming stable fcc and reinforcing phase where the two phases coexist. Hence, the aluminum elements with larger atomic radius were added to the non-equiatomic $Ni_{10}Cr_6WFe_9Ti$ HEA. A series of $Ni_{10}Cr_6WFe_9TiAlx$ alloys was designed based on the ab initio calculations and thermodynamic calculation. This paper only focuses on the $Ni_{10}Cr_6WFe_9TiAlx$ (x = 0, 1.0 and 1.5, at.%) HEAs to illustrate the proof of concept. The vacuum arc smelting technique was applied to prepare $Ni_{10}Cr_6WFe_9TiAlx$ HEAs. The effect of Al addition on the microstructure and mechanical properties of as-cast $Ni_{10}Cr_6Wfe_9TiAlx$ HEAs were investigated in detail.

2. Experimental

In this study, the investigated $Ni_{10}Cr_6Wfe_9TiAlx$ (x = 0, 1.0 and 1.5, at.%) HEAs were produced by vacuum arc melting in a water-cooled copper hearth under argon atmosphere, and the raw materials were fabricated in purities great than or equal to 99.99% (the purities of each element: Ni: 99.99%, Cr: 99.99%, W: 99.99%, Fe: 99.99%, Ti: 99.99%, Al: 99.99%, Beijing Yanbang New Material Technology Co., LTD, Beijing, China). The fabricated $Ni_{10}Cr_6Wfe_9TiAlx$ (x = 0, 1.0, and 1.5 at.%) HEAs were denoted as Al_0, $Al_{1.0}$, and $Al_{1.5}$, respectively. To improve chemical homogeneity, each ingot was remelted at least four times repeatedly. The HEAs plates of size of 65 mm × 30 mm × 10 mm were fabricated through the water-cooled copper mold.

To investigate the effect of Al on the microstructure and mechanical properties of the $Ni_{10}Cr_6WFe_9TiAl$ series HEAs, the crystal structure was determined using an X-ray

diffraction spectrometer (XRD, PANAlytical X'Pert'S-MPD, PANalytical B.V, Amsterdam, The Netherlands) with Cu–Kα (λ = 0.154056 nm) radiation at a scan speed of 5°/min. The microstructures were analyzed using scanning electron microscopy (SEM, JSM-7900F, JEOL Ltd., Tokyo, Japan) and electron backscatter diffraction (EBSD). The high-resolution microstructure and chemical composition were analyzed using transmission electron microscopy (TEM, Talos F200x, Thermo Fisher Scientific, Wilson County, TN, USA) coupled with an energy-dispersive X-ray spectrometer (EDS). For the tensile test, the nonstandardized tensile specimens (see Figure 1) were prepared from the alloy ingot by electrical discharge machining [27], and the tensile test was carried out using a servo-hydraulic Instron testing machine (INSTRON 5982, Instron Corporation, Norfolk County, MA, USA) with a strain rate of 0.2 mm/min at room temperature. The Brinell hardness tests were also measured using a Brinell hardness tester (NEXUS 8003B/HBT, Innovatest, Maastricht, The Netherlands) at a load of 5 kgf for 10 s, each sample was tested at least 10 times, and the average values were provided.

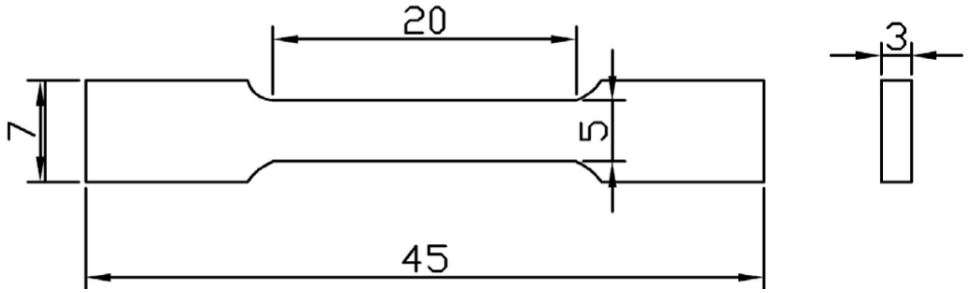

Figure 1. Dimension of tensile test specimens, data from [27].

3. Results and Discussion

Figure 2a,b represent the XRD diffraction pattern of specimens for non-equiatomic $Ni_{10}Cr_6WFe_9TiAl_x$ (x = 0, 1.0, 1.5) HEAs obtained by vacuum arc melting. As can be seen, all the alloys were composed mainly of FCC solid solution or FCC + Al_2W phase (see Figure 2a), and the total number of phases of these alloys was well below the maximum equilibrium number allowed by the Gibbs phase rule. The results showed that the high mixing entropy does facilitate the formation of simple solid solutions [28,29]. Further observation showed that the Al_0 HEA has only an FCC phase, corresponding to (111), (200), (220), and (311) lattice indices, which is not the same as those obtained with selective laser melting processes [23]. It was found that with the increase of Al content, the phase composition of these HEAs became complicated, and the increase of Al content led to the increase of Al_2W phase and the decrease of FCC phase in as-cast $Ni_{10}Cr_6WFe_9TiAlx$ HEAs, which might be related to the greater electronegativity difference between aluminum and tungsten. The phases of $Ni_{10}Cr_6WFe_9TiAlx$ HEAs were further analyzed at the Bragg angles (2 θ) of 42–54° by XRD (see Figure 1b). The XRD patterns of these alloys exhibited lower angle shift in 2 θ values of high intense peaks associated with (111) and (200) planes when compared to FCC matrix, and the successful incorporation of aluminum in FCC matrix was confirmed.

Figure 3 shows the microstructures of the as-cast $Ni_{10}Cr_6WFe_9TiAlx$ (x = 0, 1.0, 1.5) HEAs specimens under different Al content. Figure 3a–c show the representative backscattering electron image of specimens for x = 0, 1.0, and 1.5, respectively. The results showed that the microstructure of these HEAs mainly consisted of coarse-grained FCC phase or a duplex state where the FCC and Al_2W phases coexist, and the size and count of precipitates had an obvious progress with the increased Al concentration. In addition, the SEM-EDS mapping images of HEAs were shown in Figure 3d, and the analysis showed that the main elements of precipitates were Al and W, and poorer in Ni, Cr, Fe, and Ti elements. The SEM-EDS results confirmed that the precipitates was Al_2W, which is consistent with the XRD results. In addition, the precipitates were continuously distributed along the

boundaries of the matrix phase and their size was larger in $Al_{1.5}$ HEA compared to $Al_{1.0}$ HEAs (see Figure 3e).

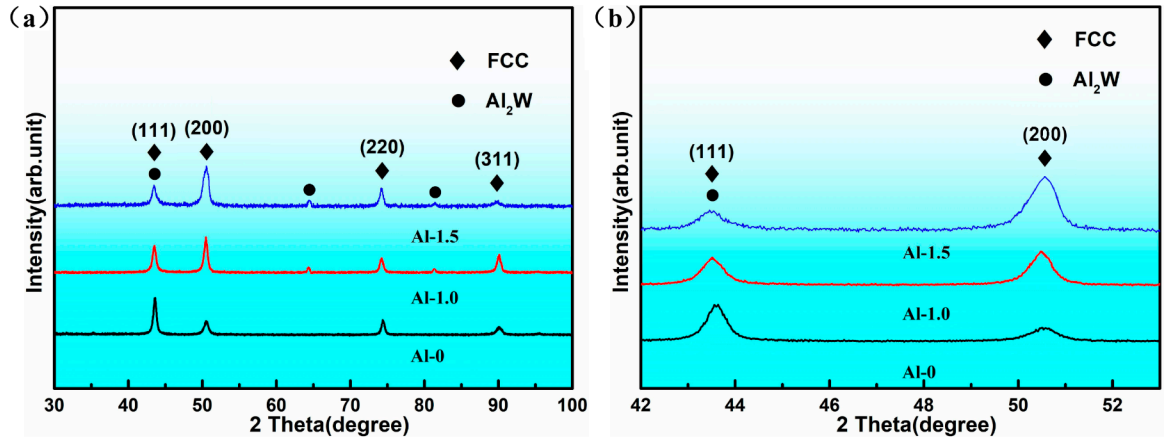

Figure 2. The XRD patterns of as-cast $Ni_{10}Cr_6WFe_9TiAlx$ (x = 0, 1.0, 1.5) HEAs (**a**) and obtained in a small range of 2 θ = 42–54° (**b**).

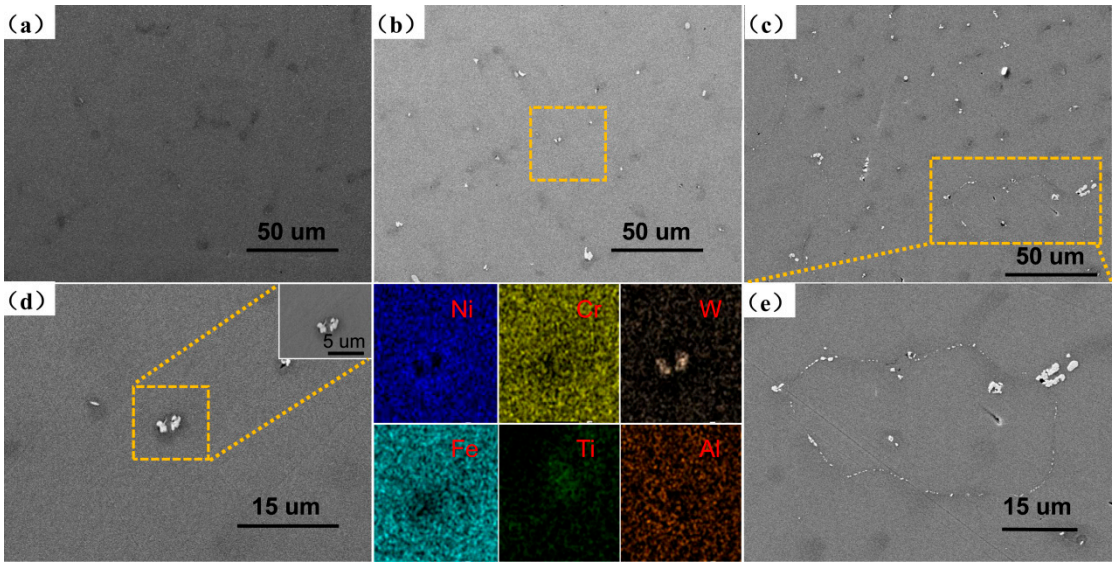

Figure 3. The microstructures of as-cast $Ni_{10}Cr_6WFe_9TiAlx$ (x = 0, 1.0, 1.5) HEAs: (**a**–**c**) a representative backscattering electron image obtained in Al_0, $Al_{1.0,}$ and $Al_{1.5}$, respectively; (**d**) the magnified images of the dashed line boxes in (**b**), and the EDS elemental maps of the Ni, Cr, W, Fe, Ti, and Al; (**e**) the magnified images of the dashed line boxes in (**c**).

Figure 4 presents the EBSD images of as-cast $Ni_{10}Cr_6WFe_9TiAlx$ (x = 0, 1.0, 1.5) HEAs specimens under different Al content. Figure 4a,c,e show the inverse pole figure (IPF) maps of specimens for x = 0, 1.0, and 1.5, respectively. In the Al_0 and $Al_{1.0}$ HEAs, both alloys consisted of coarse grains with almost random orientations, and the grain size was concentrated between 700 μm and 1000 μm with a maximum value of 1400 μm. When the Al content increased to 1.5, the grain size distribution and grain orientations of alloy had no obvious change (see Figure 4e). The results showed that the Al element has no significant influence on grain size distribution and grain orientations of $Ni_{10}Cr_6WFe_9TiAlx$ (x = 0, 1.0, 1.5) HEAs during vacuum arc melting. Then, the phase distribution map of these HEAs was analyzed (see Figure 4b,d,f). Face-centered cubic (FCC) and Al_2W are represented by red and black, respectively. The EBSD results showed that the Al_0 HEA has only FCC matrix. For the $Al_{1.0}$ HEA, the EBSD results showed that the microstructure consisted of FCC matrix and Al_2W phase, and further quantitative analysis showed that the fraction of

FCC and Al2W was 96.5% and 3.5%, respectively. When the Al mole content increased to 1.5, the fraction of FCC decreased to 92.7% and the Al_2W increased to 7.3%.

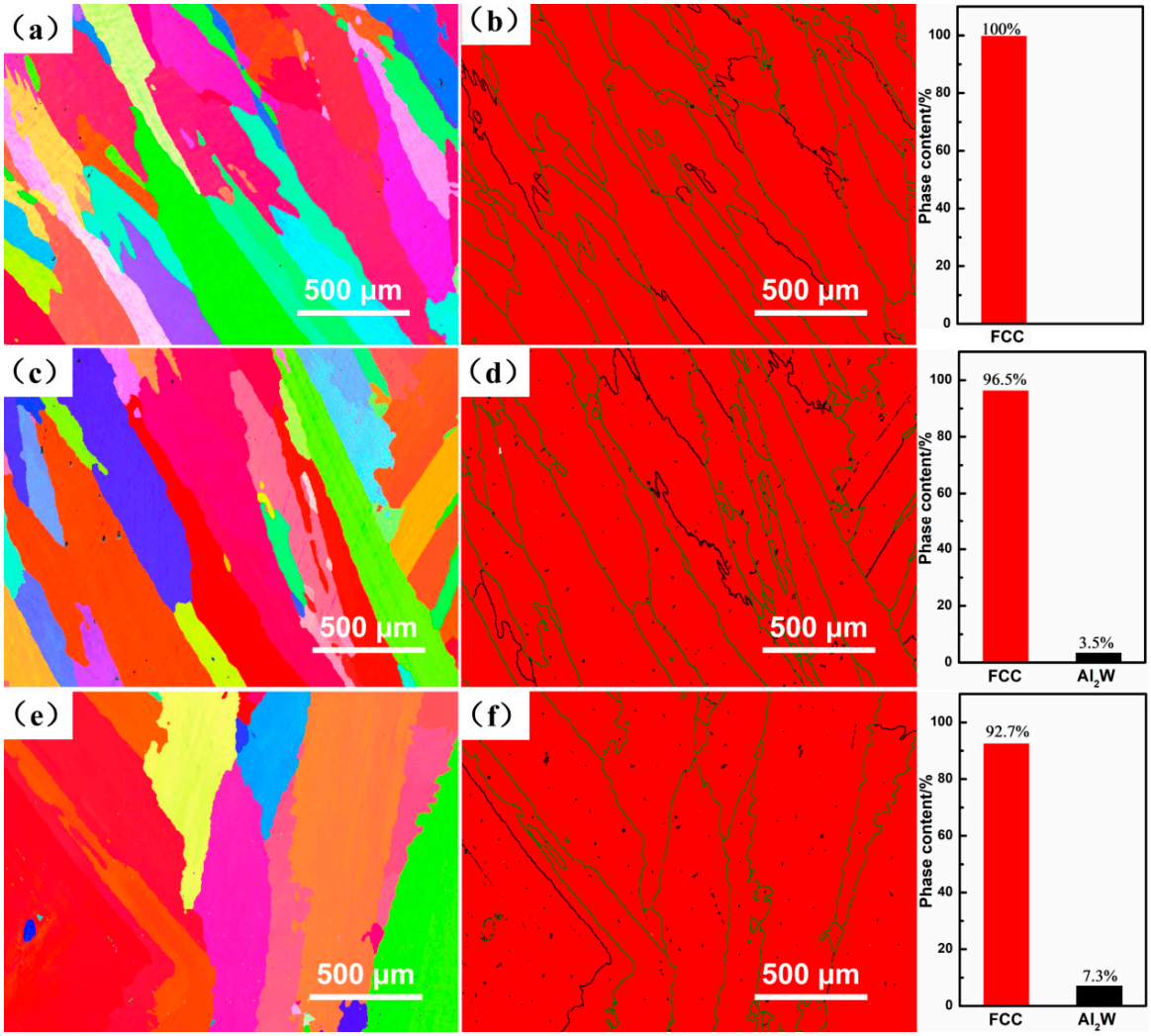

Figure 4. The EBSD images of as-cast $Ni_{10}Cr_6WFe_9TiAlx$ (x = 0, 1.0, 1.5) HEAs: (**a**,**c**,**e**) the inverse pole figure (IPF) map; (**b**,**d**,**f**) phase distribution map.

Figure 5a shows representative room temperature tensile stress–strain curves of the non-equiatomic $Ni_{10}Cr_6WFe_9TiAlx$ (x = 0, 1.0, 1.5) HEAs samples. As can be seen, the overall tensile stress–strain properties were significantly improved with the addition of Al. The $Al_{1.0}$ HEA exhibited high ultimate tensile strength and total elongation of ~741 MPa and ~46%, respectively, which exhibited its excellent comprehensive mechanical properties. These values corresponded to a ~15.1% increase in ultimate tensile strength, while the total elongation decreased by ~9.8%, compared with the Al_0 HEA (ultimate tensile strength of ~644 MPa and total elongation of ~51%). When the Al mole content increased to 1.5, the ultimate tensile strength (~671 MPa) and total elongation (~19%) decreased significantly. Figure 5b shows the change in hardness value of the non-equiatomic $Ni_{10}Cr_6WFe_9TiAlx$ (x = 0, 1.0, 1.5) HEAs. With increasing Al content, the hardness value of these HEAs showed a gradually increasing trend. The average hardness of the $Al_{1.0}$ HEA was about 238.2 ± 2.5 HBW, which was significantly higher than that of the Al_0 HEA (~190.4 ± 3.0 HBW). This is because the aluminum atomic random distribution and its larger atomic radius cause serious lattice distortion within the FCC structure, which contributes to the enhanced hardness. Compared with the $Al_{1.0}$ HEA, the $Al_{1.5}$ HEA had a similar hardness (~245.5 ± 4.3 HBW), and the reasons for the increase in hardness were the Al elemental concentrations significantly above

the solid solubility limit and the Al_2W particles forming simultaneously in the matrix, which results in the improvement of hardness.

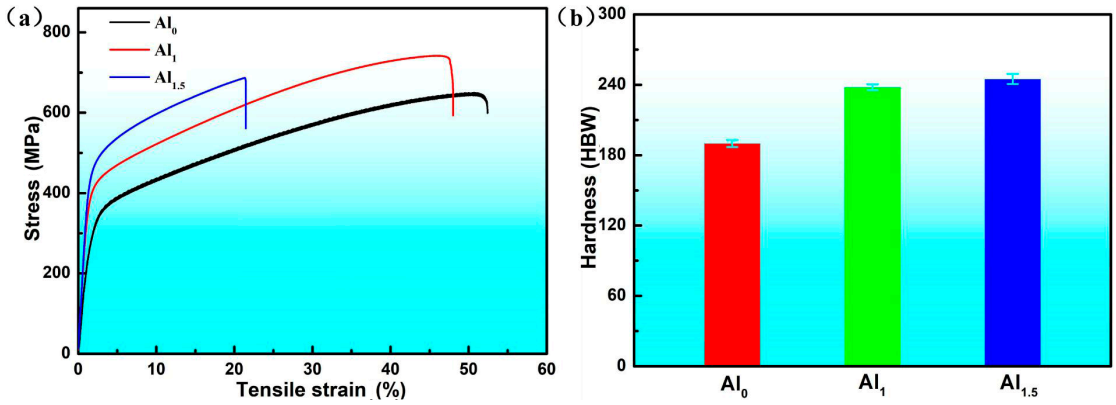

Figure 5. The mechanical properties of as-cast $Ni_{10}Cr_6WFe_9TiAlx$ (x = 0, 1.0, 1.5) HEAs: (**a**) Room temperature tensile stress–strain curves of alloys; (**b**) the Brinell hardness of alloys.

Figure 6 shows the tensile fractured surfaces of as-cast $Ni_{10}Cr_6WFe_9TiAlx$ (x = 0, 1.0, 1.5) HEAs. The results showed that the fracture surfaces of Al_0 HEA and $Al_{1.0}$ HEA were relatively uniform, and the presence of dimples with uniform distribution can be observed from the enlarged views of Figure 6b,e. The fractured surfaces were mainly composed of microsized dimples of ~20 μm, indicating that the fracture mode of the two HEAs is ductile fracture. In addition, some pores (yellow arrows) and cracks (red arrows) appeared on the sample surface in $Al_{1.0}$ HEA, which was one of the factors for the decrease of ductility. With the increase of Al element content, the fracture morphology of $Al_{1.5}$ HEA possessed morphology with river pattern and brittle fracture surface (blue arrows), which had brittle fracture characteristics. These conditions were mainly caused by the acceleration of coarse Al_2W phase formation, resulting in the material changing from plasticity to brittleness and a decrease in mechanical property.

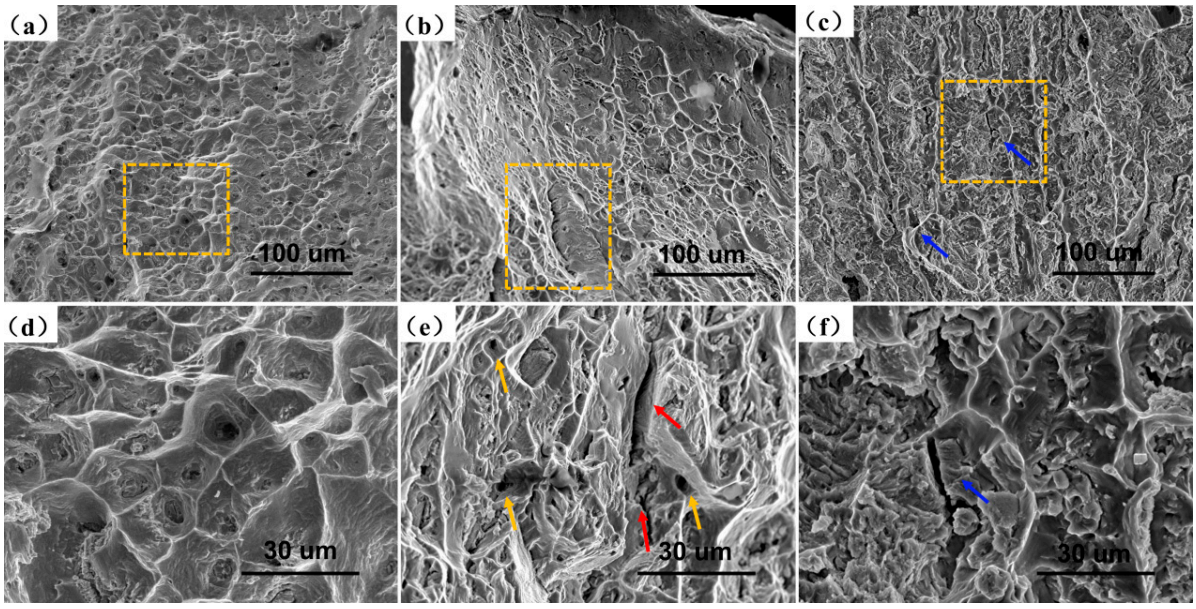

Figure 6. Tensile fractography of as-cast $Ni_{10}Cr_6WFe_9TiAlx$ (x = 0, 1.0, 1.5) HEAs (**a**–**c**), and (**d**–**f**) are the magnified images of the dashed line boxes in (**a**–**c**). The pores of tensile fractured surfaces are indicated by yellow arrows, the cracks of tensile fractured surfaces are indicated by red arrows, the brittle fracture surface is indicated by blue arrows.

To further reveal the deformation mechanism underlying the excellent mechanical properties of the current alloy, TEM analysis were conducted for the $Ni_{10}Cr_6WFe_9TiAlx$ (x = 0, 1.0, 1.5) HEAs before and after the tensile testing, and the results are shown in Figure 7. In the as-cast $Al_{1.0}$ HEA, a small number of dislocations were generated (see Figure 7a), attributed to stress resulting from rapid solidification during preparation. Likewise, the observed dislocations in the other two alloys (Al_0 HEA and $Al_{1.5}$ HEA) were almost the same as $Al_{1.0}$ HEA. Figure 7b presents the bright field TEM images of deformed $Al_{1.0}$ HEA; a large number of dislocation were formed due to the large deformation, and this dislocation formed multiple arrays of dislocations parallel to each other through the planar slip mechanism. Likewise, the observed dislocation in the other two alloys (Al_0 HEA and $Al_{1.5}$ HEA) were almost the same as $Al_{1.0}$ HEA. In addition, the severely deformed grains containing high density of stacking faults (SFs) were found inside $Al_{1.0}$ HEA (see Figure 7c), which resulted in the formation of nano-spaced SF networks. Further observation showed that Al_2W particles were severely stretched and cut by the SF intersections, indicating that the shearable precipitates have excellent cooperative deformation capacity [30,31].

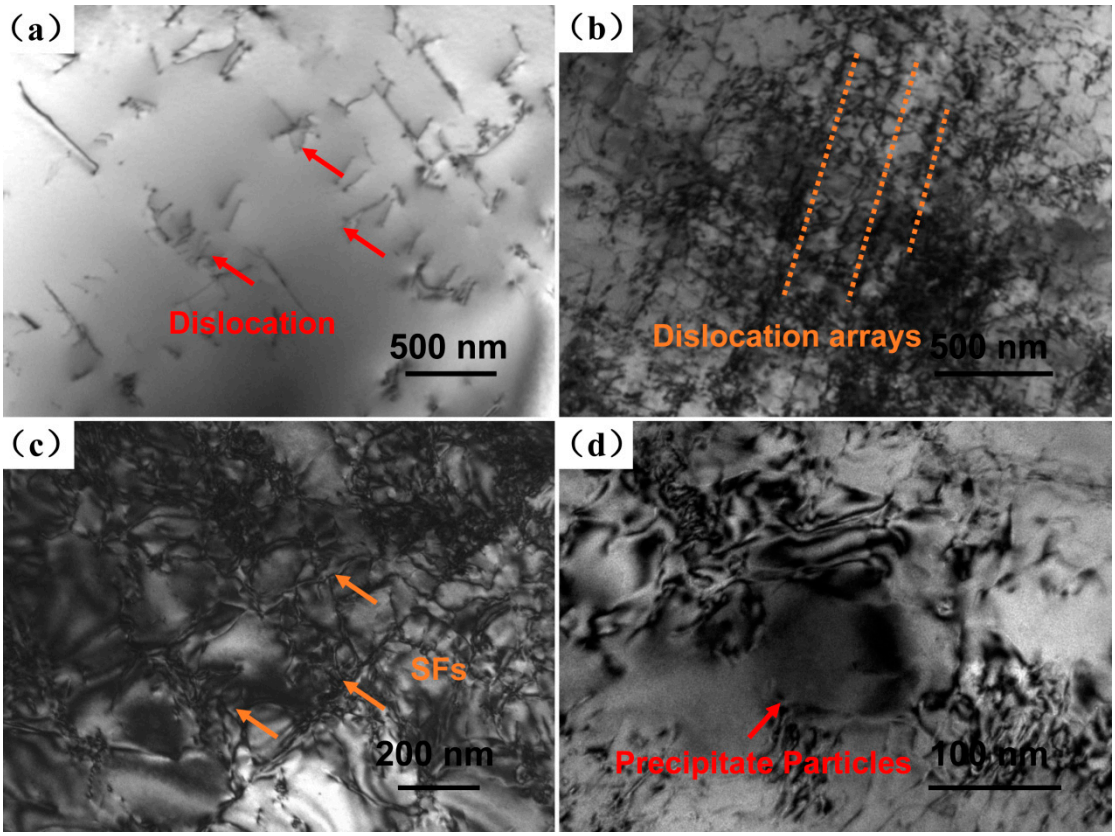

Figure 7. TEM images of $Al_{1.0}$ HEA: (**a**) bright field (BF) TEM images of as-cast $Al_{1.0}$ HEA; (**b**) bright field (BF) TEM images of deformed $Al_{1.0}$ HEA; (**c**,**d**) high-density SFs and stretched precipitates in the severe plastic deformation.

4. Conclusions

In this study, the non-equiatomic $Ni_{10}Cr_6WFe_9Ti$ alloys were successfully manufactured via doping Al elements that enabled the control of phase stability. The results show that the HEAs are composed mainly of FCC with Al_2W phase. The increase of Al content promotes the formation of the Al_2W phase. The $Ni_{10}Cr_6WFe_9TiAl$ HEA material achieved superior mechanical properties. The ultimate tensile strength and total elongation were determined as 741 MPa and 46%, respectively. The improvement in the mechanical properties of the $Ni_{10}Cr_6WFe_9TiAl$ HEA is mainly attributed to the precipitation strengthening of the

high-density Al_2W phase. This work provides a reference for the future design of Al_2W precipitation-strengthened non-equiatomic HEAs with ideal properties.

Author Contributions: Conceptualization, data curation, writing—original draft, X.Y. and L.H.; writing—review and editing, E.L.; investigation, data curation, C.Y. All authors have read and agreed to the published version of the manuscript.

Funding: This research was funded by the Natural Science Research Project of Shaanxi Province, grant number 2022JQ-505. And the APC was funded by Xi'an Technological University.

Acknowledgments: This work was supported by the Natural Science Research Project of Shaanxi Province (Nos. 2022JQ-505).

Conflicts of Interest: The authors declare no conflict of interest.

References

1. Hsu, W.C.; Shen, T.E.; Liang, Y.C.; Yeh, J.W.; Tsai, C.W. In situ analysis of the Portevin-Le Chatelier effect from low to high-entropy alloy in equal HfNbTaTiZr system. *Acta Mater.* **2023**, *253*, 118981. [CrossRef]
2. Zhang, H.; Liu, G.; Ren, N.N.; Cheng, N.; Dong, Z.X.; Ma, Q.S. Microstructure evolution and high temperature wear resistance of in-situ synthesized carbides reinforced NiCoFeCrSiMo high entropy alloy coatings fabricated by laser cladding. *Surf. Coat. Tech.* **2023**, *464*, 129573. [CrossRef]
3. Xu, T.; Chen, Q.J.; Ji, L.; Zheng, Z.D.; Wang, K.; Liu, H.Y. BCC/B2 structure and dislocation strengthening behavior in high Ti content TiAlVCrNb high-entropy alloys. *J. Alloys Compd.* **2023**, *956*, 170179. [CrossRef]
4. Li, J.L.; Zhou, G.; Han, J.K.; Peng, Y.H.; Zhang, H.Y.; Zhang, S.; Chen, L.; Cao, X. Dynamic recrystallization behavior of single-phase BCC structure AlFeCoNiMo0.2 high-entropy alloy. *J. Mater. Sci. Technol.* **2023**, *23*, 4376–4384. [CrossRef]
5. Yang, X.G.; Zhou, Y.; Zhu, R.H.; Xi, S.Q.; He, C.; Wu, H.; Gao, Y. A Novel, Amorphous, Non-equiatomic FeCrAlCuNiSi High-Entropy Alloy with Exceptional Corrosion Resistance and Mechanical Properties. *Acta Metall. Sin. (Engl. Lett.)* **2019**, *10*, 1–7. [CrossRef]
6. Yang, Y.; Chen, T.; Tan, L.; Poplawsky, J.D.; An, K.; Wang, Y.; Samolyuk, G.D.; Littrell, K.; Lupini, A.R.; Borisevich, A.; et al. Bifunctional nanoprecipitates strengthen and ductilize a medium entropy alloy. *Nature* **2021**, *595*, 245–249. [CrossRef]
7. Chong, K.; Gao, Y.; Zhang, Z.B.; Zou, Y.; Liang, X.B. Thermal stability and corrosion behavior of a novel Zr22.5Ti22.5Hf22.5Ni22.5Ta10 high-entropy amorphous alloy. *Corros. Sci.* **2023**, *213*, 110979. [CrossRef]
8. Li, X.F.; Liu, Y.; Cui, Y.; Zhang, J.; Fu, J.X. Microstructural evolution and tensile property of gradient microstructure CoCrFeMnNi high-entropy alloy induced by pre-torsion. *J. Alloys Compd.* **2023**, *955*, 170053. [CrossRef]
9. Lin, W.T.; Chen, D.; Dang, C.Q.; Yu, P.J.; Wang, G.; Lin, J.H.; Meng, F.L.; Yang, T.; Zhao, Y.L.; Liu, S.F.; et al. Highly pressurized helium nanobubbles promote stacking-fault-mediated deformation in FeNiCoCr high-entropy alloy. *Acta Mater.* **2021**, *210*, 116843. [CrossRef]
10. Chen, H.Y.; Gou, J.M.; Jia, W.T.; Song, X.; Ma, T.Y. Origin of hard magnetism in Fe-Co-Ni-Al-Ti-Cu high-entropy alloy: Chemical shape anisotropy. *Acta Mater.* **2023**, *246*, 118702. [CrossRef]
11. Liu, K.; Wang, J.Y.; Li, X.; Qin, Q.; Wu, S.J.; Yu, H.C. A new lightweight Al2.7TiVCrCu high entropy alloy with excellent strength and toughness after homogenization treatment. *Sci. Eng. A* **2023**, *869*, 144779. [CrossRef]
12. Wei, Q.; Zhang, A.J.; Han, J.S.; Xin, B.B.; Su, B.; Wang, X.; Meng, J. A novel $Hf_{30}Nb_{25}Ta_{25}Ti_{15}Mo_5$ refractory high entropy alloy with excellent combination of strength and ductility. *Sci. Eng. A* **2022**, *857*, 144035. [CrossRef]
13. Fan, R.; Wang, L.P.; Zhao, L.L.; Wang, L.; Zhao, S.C.; Zhang, Y.J.; Cui, B. Synergistic effect of Nb and Mo alloying on the microstructure and mechanical properties of CoCrFeNi high entropy alloy. *Sci. Eng. A* **2022**, *829*, 142153. [CrossRef]
14. Song, Y.P.; Yan, L.C.; Pang, X.L.; Su, Y.J.; Qiao, L.J.; Gao, K.W. Effects of co-alloying Al and Cu on the corrosion behavior and mechanical properties of nanocrystalline FeCrNiCo high entropy alloys. *Corros. Sci.* **2023**, *213*, 110983. [CrossRef]
15. Hu, R.; Du, J.H.; Zhang, Y.J.; Ji, Q.X.; Zhang, R.R.; Chen, J.X. Microstructure and corrosion properties of AlxCuFeNiCoCr(x = 0.5, 1.0, 1.5, 2.0) high entropy alloys with Al content. *J. Alloys Compd.* **2022**, *921*, 165455. [CrossRef]
16. Kang, J.J.; Niu, Y.; Zhou, Y.K.; Fan, Y.X.; Ma, G.Z. Wear Resistance Prediction of AlCoCrFeNi-X (Ti, Cu) High-Entropy Alloy Coatings Based on Machine Learning. *Metals* **2023**, *13*, 939. [CrossRef]
17. Zhang, K.G.; Yin, D.Q.; Wang, B.; Li, M.C.; Xiao, X.; Ma, N.; Zhang, K.K. Ultrasonic Cavitation Erosion Behavior of CoCrxFeMnNi High-Entropy Alloy Coatings Prepared by Plasma Cladding. *Metals* **2023**, *13*, 515. [CrossRef]
18. Chuang, M.H.; Tsai, M.-H.; Wang, W.-R.; Lin, S.-J.; Yeh, J.-W. Microstructure and wear behavior of AlxCo1.5CrFeNi1.5Tiy high-entropy alloys. *Acta Mater.* **2011**, *59*, 6308–6317. [CrossRef]
19. Wang, T.T.; Jiang, W.T.; Wang, X.H.; Jiang, B.; Rong, C.; Wang, Y.; Yang, J.; Zhu, D. Microstructure and properties of Al0.5NbTi3VxZr2 refractory high entropy alloys combined with high strength and ductility. *J. Mater. Res. Technol.* **2023**, *24*, 1733–1743. [CrossRef]
20. Wei, C.B.; Lu, Y.P.; Wang, T.M.; Liaw, P.K. Microstructures and mechanical behavior of non-equiatomic Co29Cr29Fe29Ni13-xVx high-entropy alloys at room and cryogenic temperatures. *Sci. Eng. A* **2023**, *865*, 144611. [CrossRef]

21. Osintsev, K.A.; Konovalov, S.V.; Gromov, V.E.; Ivanov, Y.F.; Panchenko, I.A. Microstructure and mechanical properties of non-equiatomic Co25.4Cr15Fe37.9Mn3.5Ni16.8Si1.4 high-entropy alloy produced by wire-arc additive manufacturing. *Mater. Lett.* **2022**, *312*, 131675. [CrossRef]
22. Xu, Z.J.; Li, Z.T.; Tong, Y.; Zhang, W.D.; Wu, Z.G. Microstructural and mechanical behavior of a CoCrFeNiCu4 non-equiatomic high entropy alloy. *J. Mater. Sci. Technol.* **2021**, *60*, 35–43. [CrossRef]
23. Liang, F.; Du, J.; Su, G.S.; Xu, C.H.; Zhang, C.Y.; Kong, X.M. Phase Stability and Mechanical Properties Analysis of AlCoxCrFeNi HEAs Based on First Principles. *Metals* **2022**, *12*, 1860. [CrossRef]
24. Semenyuk, A.; Povolyaeva, E.; Sanin, V.; Zherebtsov, S.; Stepanov, N. Effect of Nitrogen Doping on the Structure and Mechanical Properties of the Fe40Mn40Cr10Co10 High-Entropy Alloy. *Metals* **2022**, *12*, 1599. [CrossRef]
25. Guo, Q.W.; Hou, H.; Pan, Y.; Pei, X.L.; Song, Z.; Liaw, P.K.; Zhao, Y.H. Hardening-softening of Al0.3CoCrFeNi high-entropy alloy under nanoindentation. *Mater. Des.* **2023**, *231*, 112050. [CrossRef]
26. Yang, X.G.; Zhou, Y.; Yang, Z.; Zhou, Y.H.; Yang, X.; Li, Y. Achieving high strength and ductility in $Ni_{10}Cr_6WFe_9Ti$ high entropy alloy by regulating lattice distortion. *Mater. Lett.* **2023**, *330*, 133394. [CrossRef]
27. Yang, X.G.; Zhou, Y.; Xi, S.Q.; Chen, Z.; Wei, P.; He, C.; Li, T.T.; Gao, Y.; Wu, H. Additively manufactured fine grained Ni6Cr4WFe9Ti high entropy alloys with high strength and ductility. *Mater. Sci. Eng. A* **2019**, *767*, 138394. [CrossRef]
28. Xiong, K.; Huang, L.; Wang, X.F.; Yu, L.; Feng, W. Cooling-Rate Effect on Microstructure and Mechanical Properties of Al0.5CoCrFeNi High-Entropy Alloy. *Metals* **2022**, *12*, 1254. [CrossRef]
29. Cao, X.; Wu, C.J.; Liu, Y.; Peng, H.P.; Su, X.P. Eutectic Reaction and Microstructure Stability in CoCrFeNiNbx High-Entropy Alloys. *Metals* **2022**, *12*, 756. [CrossRef]
30. Hemphill, M.A.; Yuan, T.; Wang, G.Y.; Yeh, J.W.; Tsai, C.W.; Chuang, A.; Liaw, P.K. Fatigue behavior of $Al_{0.5}CoCrCuFeNi$ high entropy alloys. *Acta Mater.* **2012**, *60*, 5723–5734. [CrossRef]
31. Lee, D.H.; Seok, M.Y.; Zhao, Y.; Choi, I.C.; He, J.Y.; Lu, Z.; Suh, J.-Y.; Ramamurty, U.; Kawasaki, M.; Langdon, T.G.; et al. Spherical nanoindentation creep behavior of nanocrystalline and coarse-grained CoCrFeMnNi high-entropy alloys. *Acta Mater.* **2016**, *109*, 314–322. [CrossRef]